materials

MDPI

Article

Nitrogen-Doped Nanoporous Anodic Stainless Steel Foils towards Flexible Supercapacitors

Wenlei Zhang [1], Jianle Xu [1,*], Gang Li [1,*] and Kaiying Wang [1,2]

[1] Institute of Energy Innovation, College of Materials Science and Engineering & College of Information and Computer, Taiyuan University of Technology, Taiyuan 030024, China; zhangwenlei@tyut.edu.cn (W.Z.); wangkaiying@tyut.edu.cn (K.W.)
[2] Department of Microsystems-IMS, University of South-Eastern Norway, 3184 Horten, Norway
* Correspondence: xujianle@tyut.edu.cn (J.X.); ligang02@tyut.edu.cn (G.L.)

Abstract: In this work, we report the fabrication and enhanced supercapacitive performance of nitrogen-doped nanoporous stainless steel foils, which have been prepared by electrochemical anodization and subsequent thermal annealing in ammonia atmosphere. The nanoporous oxide layers are grown on type-304 stainless steel foil with optimal thickness ~11.9 μm. The N-doped sample exhibits high average areal capacitance of 321.3 mF·cm^{-2} at a current density of 1.0 mA·cm^{-2}, 3.6 times of increment compared with untreated one. Structural and electrochemical characterizations indicate that the significant enhancement is correlated to the high charge transfer efficiency from nitriding nanosheet products Fe_3N. Our report here may provide new insight on the development of high-performance, low-cost and binder-free supercapacitor electrodes for flexible and portable electronic device applications with multiple anions.

Keywords: stainless steel foil; anodic oxidation; nitrogen doping; nanoporous structure; supercapacitors

Citation: Zhang, W.; Xu, J.; Li, G.; Wang, K. Nitrogen-Doped Nanoporous Anodic Stainless Steel Foils towards Flexible Supercapacitors. *Materials* **2022**, *15*, 1615. https://doi.org/10.3390/ma15041615

Academic Editors: Junwei Wu and Yanan Chen

Received: 20 December 2021
Accepted: 18 February 2022
Published: 21 February 2022

1. Introduction

With rapid growth of global population and high spread of electronic devices, the demanding for energy storage devices and technologies have stimulated high interests towards research and development from academia and industry sectors [1,2]. As the forefront of electrical energy storage system, supercapacitor shows prominent advantages such as fast charging/discharging, high power density, and long cycle life [3], making it promising in the area like portable electronics and hybrid electric vehicles [4]. Among various electrode materials, stainless steel (SS) based devices are receiving more and more attention recently, contributed by its low-cost, binder-free structure, advantageous mechanical property, and reliable conductivity [5].

Although much research has been devoted to the usage of SS served as substrate or collector [6–8], little literature is available on the fabrication of SS-based supercapacitor, taking advantages of good supercapacitive performance from Fe_2O_3 [9] or Fe_3O_4 [10]. Among them, Sagu et al. [11] made wire-like nanoporous structure on the surface of bulk SS by anodic oxidation method, for a capacitance of 18 mF·cm^{-2} in NaOH electrolyte. Deshmukh et al. [12] thermally oxidized type-304 SS mesh in ambient air atmosphere at a temperature up to 800 °C, with a result of 45.92 mF·cm^{-2} average capacitance. Long et al. [13] explored lithium storage and supercapacitive performance of thermally oxidized type-304 SS mesh. However, due to their relatively small specific surface area and limited conductivity, the capacitance value was still far away from applications.

Recently, mixed-anion compounds, conductive polymer compounds or compounding metals with multiple anions beyond the single-oxide ion, offered a new platform for the superior functional materials [14–16]. The replacement of oxygen atoms with other anion like nitrogen, sulfur or phosphorus can narrow the bandgap [17], increase vacancies within

their crystal structures, and led to high conductivity and good ionic diffusion [18]. Thus, the supercapacitive performance of oxidized SS is willing to be enhanced by the doping process.

Considering the issues raised above, we fabricated an ultra-thick nanoporous oxide layer on the surface of type-304 stainless steel foil by pulsed anodic oxidation method with different applied voltages [19]. A nitrogen doping process was carried out for enhancing capacitance and cycling stability. The samples before and after nitrogen doping have been investigated by structural characterization and electrochemical measurements to deeply understand their correlation among porous structures, constituent components, as well as enhanced electrochemical behaviors.

2. Materials and Methods

2.1. Synthesis Methods

Nanoporous anodized stainless steel (NASS) sample was synthesized through anodic oxidation method. Prior to oxidation process, the SS foils (type-304, Shanghai Shida Stainless Steel Co., Ltd., Shanghai, China) with dimensions of 10.0 mm × 20.0 mm × 0.1 mm were ultrasonicated in acetone, ethanol, and DI water for 10 min, respectively. The anodic oxidation was performed in a two-electrode electrochemical cell with the SS foil as the working electrode and a graphite plate as the counter electrode. The electrolyte was made by a mixture of 111 g ethylene glycol ($C_2H_6O_2$ 99.5%, Sinopharm Chemical Reagent Co., Ltd., Shanghai, China), 0.37 g ammonium fluoride (NH_4F 95.0%, Sinopharm Chemical Reagent Co., Ltd.) and 0.18 g H_2O. To optimize the supercapacitive performance of NASS, three different potentials, 30, 50 and 70 V were applied with the oxidation time of 2 h at room temperature. The synthesized NASS samples were rinsed in acetone and DI water several times, and then annealed at 500 °C in air for 2 h to stabilize their nanoporous structure. Some NASS samples were further treated under ammonia atmosphere at 500 °C for 1 h to fabricate the nitrogen doped (NASS-N) samples.

2.2. Characterization Techniques

The surface morphology of NASS and NASS-N samples were examined using a field emission scanning electron microscopy (FESEM, Hitachi SU8010, Tokyo, Japan). A small amount of powder was scratched from stainless-based samples. The powder was further mixed with ethanol followed by 15 mins' ultrasonic dispersion, forming a homogeneous solution for further transmission electron microscope (TEM, JEOL JEM-2100F, Tokyo, Japan) observation. The crystal structures were tested by an X-ray diffraction (XRD, Rigaku SmartLab 9, Tokyo, Japan) in the 2θ range of 10–70 degree with CuKα (λ = 1.54 Å) radiation. The chemical analysis was evaluated under an X-ray photoelectron spectroscopy (XPS, Thermo VG Escalab 250Xi, New York, NY, USA). The elemental compositions and species were studied through an energy dispersive spectrometry (EDS, Hitachi SU8010, Tokyo, Japan) equipped in the same SEM.

2.3. Electrochemical Measurements

The supercapacitive performance of NASS and NASS-N samples was examined by cyclic voltammetry (CV), electrochemical impedance spectra (EIS) and galvanostatic charge-discharge (GCD) tests employing an electrochemical workstation (Zahner IM6, Kronach, Germany). All the tests were under a standard three-electrode system, where the fabricated samples, platinum mesh and Ag/AgCl were used as working, counter and reference electrode, respectively. 1.0 M Na_2SO_4 neutral aqueous solution was served as electrolyte in the electrochemical measurements.

3. Results and Discussion

Figure 1a shows a typical top-view SEM micrograph of NASS sample. After the anodic oxidation process, a homogenous nanoporous structure was obtained from the surface of SS foil. The lower magnified SEM image is shown in Figure S1 of the Supplementary Materials. According to our previous research, the fabrication process can be explained

by the competitive steady state between the oxidation of SS foil and electric field assisted etching of barrier layer, as well as the selective dissolution of Ni oxide in the SS anodic oxidation process [19,20]. Figure 1b–d exhibit the high magnification SEM images of NASS samples with three different anodic potentials. It proved that the pore size can be adjusted through the applied potential during oxidation process. 30 V, 50 V and 70 V oxidized samples had the value of approximate 35, 50 and 55 nm respectively, and increased with the increasing of applied potential. This result had a good agreement with other reports [21,22]. However, higher (70 V) or lower (30 V) potentials may bring some defects, such as the over-etched holes, compact oxide layer or inefficient-etched areas [23], leading to an adverse impact to the supercapacitive performance of NASS.

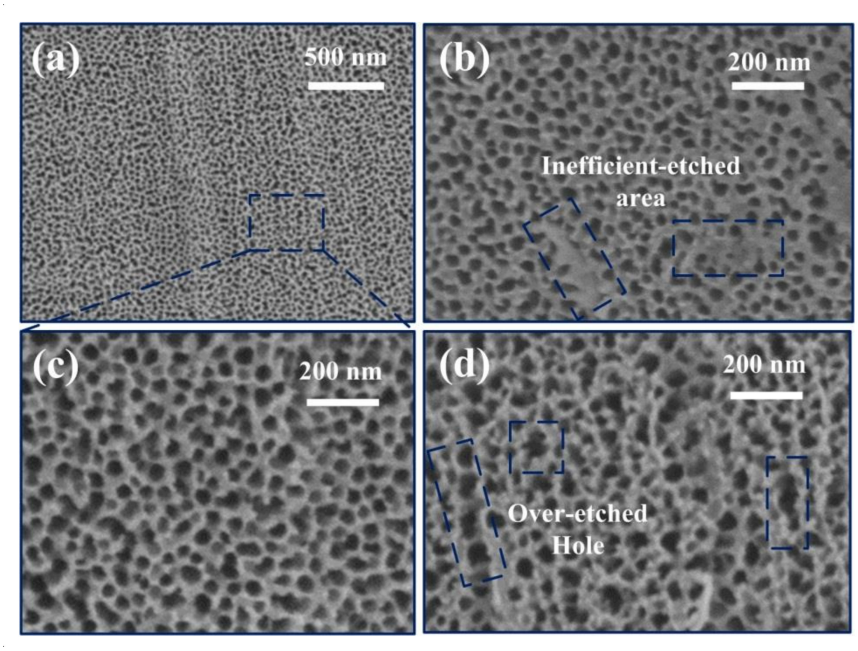

Figure 1. SEM graphs of NASS samples with different anodic oxidation potential. (**a**) The overview graph of NASS sample with applied potential of 50 V. (**b**–**d**) The high magnification graph of NASS sample with applied potential of (**b**) 30 V, (**c**) 50 V and (**d**) 70 V.

Figure 2a presents the FESEM graph of 50 V anodic sample after nitrogen doping process in the ammonia atmosphere. The NASS-N sample shows a regular nanoporous structure with the approximate pore size of 50 nm and pore wall thickness of 15 nm. No obvious deformation or addition was found on the structure. Figure 2b shows the cross-sectional view of NASS-N sample. An NASS-N film with thickness ~11.9 μm was successfully fabricated in this work, so far, is the thickest nanoporous Fe-based layer in reported literature, which in principle could offer large surface area and most active materials for electrochemical supercapacitive electrodes [24,25]. TEM was also performed to investigate the microstructure of NASS-N. As shown in Figure 2c, some large nanosheets can be found with the interplanar spacing of 0.49 nm, corresponding to the (111) plane of Fe_3O_4 phase (0.489 nm) [26] from the anodic oxidation process of SS foil. The smaller lattice spacing was measured as 0.27 nm, corresponding to the (110) plane of the Fe_3N phase (0.269 nm) [27]. The result proves that the nitrogen atoms were actually doped into the oxide layer and formed the stable Fe_3N crystal structure.

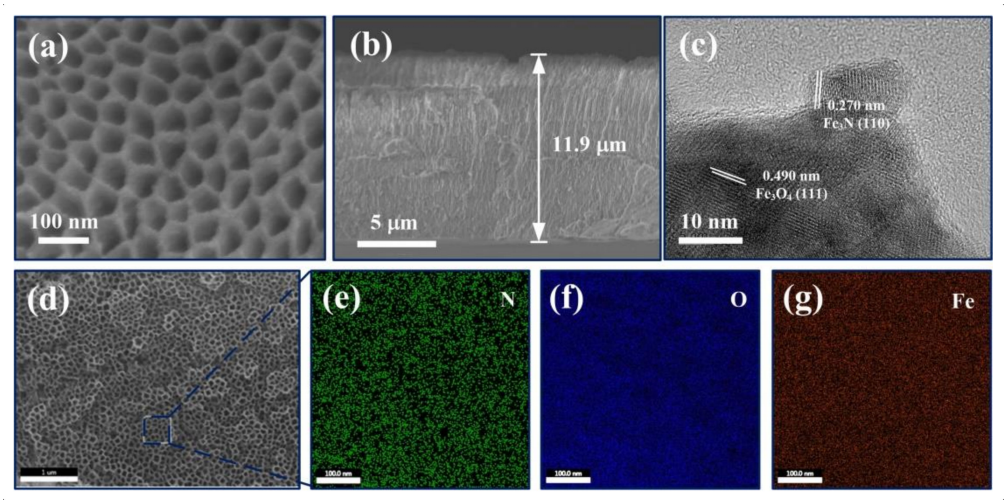

Figure 2. Characterization graphs of NASS-N samples. (**a**) High magnification SEM graph of the sample surface. (**b**) SEM graph of the sample side-wall. (**c**) TEM graph. (**d**–**g**) SEM-EDS graphs.

The phase and composition of NASS-N are characterized by SEM-EDS, XRD and XPS. The SEM-EDS elemental mapping of NASS-N is shown in Figure 2d–g, which confirmed that the N, O and Fe were distributed uniformly and homogeneously across the NASS-N sample. Figure 3a presents the XRD patterns of NASS and NASS-N samples. Both of them exhibit characteristic peaks of Fe_2O_3 at 24.1° (012), 33.2°(104), 41.2°(113), 49.3° (024) and 54.3° (116) (JCPDS No. 33-0664). After the nitrogen doping process (NASS-N), several new peaks appeared at 28.7°, 30.3° and 57.5°, corresponding to (101), (110) and (112) of Fe_3N (JCPDS No. 49-1663). These data provide the evidence that some stable Fe_3N crystals were generated during nitridation process, which shows a good agreement with the observation result from TEM. Moreover, the peak intensity of Fe_3O_4 at 18.5° (111), 37.4° (222) and 57.5° (511) (JSPDS No. 75-0449) increased significantly after nitridation. This can be explained as the production of Fe_3O_4 from Fe_2O_3 by the reduction of ammonia at a relatively high temperature of 500 °C. Further information on the chemical composition and surface electronic state of NASS and NASS-N was acquired from XPS. As shown in Figure 3b, Fe 2p, Cr 2p, C 1s and O 1s peaks in the survey XPS spectrum present the original composition of oxidized SS foil. The relatively weak Ni 2p peak in NASS-N sample was resulted from the selectivity etching of Ni oxides during anodization [19]. A characteristic N 1s peak was observed in NASS-N sample, confirming the successful nitridation process. Figure 3c presents the O 1s spectra of NASS and NASS-N. It can be found that both of the spectra can be divided into two peaks at 530.5 eV and 532.1 eV, corresponding to the adsorbed oxygen and the crystal oxygen respectively. Long et al. [13] discussed that the adsorbed oxygen peak related directly to the defects, and thus increased the conductivity of the samples. Since the intensity ratio between adsorbed oxygen peak and crystal oxygen peak of NASS-N sample (0.85) was larger than that of NASS sample (0.77), its conductivity of NASS-N may also be improved, and then promoted its electrochemical performance. The Fe 2p spectrum of NASS-N sample (Figure 3d) shows two predominant peaks at 711.3 eV (Fe 2p3/2) and 725.3 eV (Fe 2p1/2) with a shake-up satellite peak at 720.1 eV. The former two peaks were the characteristic peaks of Fe^{3+}, while the satellite peak suggesting the presence of Fe_3N after nitrogen doping [28]. This result was also in line with the high-resolution N 1s spectrum of NASS-N sample. As shown in Figure 3e, two peaks with the binding energy of 400.1 eV and 402.9 eV were observed, demonstrating the existence of O-Metal-N and Metal-N, respectively [29]. The above SEM-EDS, XRD and XPS results indicated the successful nitridation process of NASS-N sample collectively.

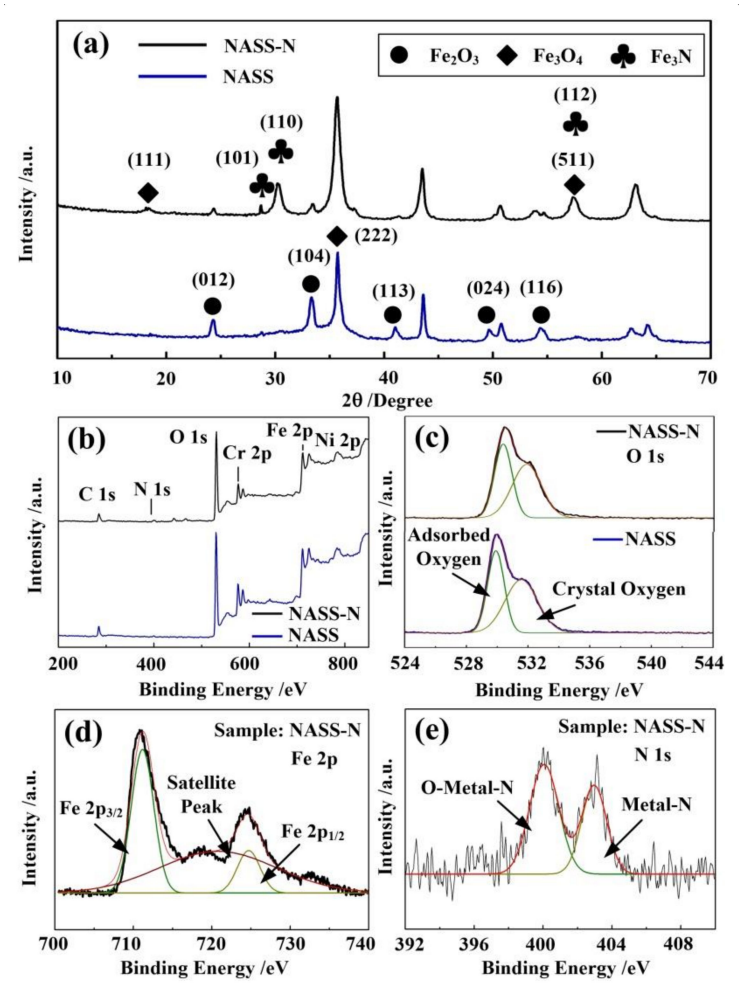

Figure 3. XRD and XPS patterns of NASS and NASS-N samples. (**a**) XRD spectrums. (**b**) XPS survey spectrum. (**c**–**e**) High resolution XPS spectrum of (**c**) O 1s, (**d**) Fe 2p and (**e**) N 1s.

Electrochemical Measurements were carried out to evaluate the capacitive performance of NASS samples with different anodic fabrication potentials. Figure 4a shows the CV curves of NASS samples anodized at 30 V, 50 V and 70 V with the scan rate of 100 $mV \cdot s^{-1}$, voltage window of −0.8–0 V. The CV curves had a quasi-rectangular shape without distinct redox peak, indicating the electrical double-layer capacitance (EDLC) characteristic of the electrodes [13,30]. Moreover, the 50 V oxidized sample exhibited a larger integrated area and higher current response than the other two, showing the optimized capacitive behavior. Representative GCD curves of these samples obtained at a current density 1 $mA \cdot cm^{-2}$ are presented in Figure 4b. The average areal capacitance of these three samples were 51.3 $mF \cdot cm^{-2}$, 90.0 $mF \cdot cm^{-2}$ and 62.5 $mF \cdot cm^{-2}$ (discharge time was 41 s, 72 s and 50 s respectively) calculated from GCD curves [31]. This result can be explained from the SEM observation results. With lower applied potential, the oxidation process of SS was not enough, leading to the smaller surface area and thinner oxide layer. The lack of active material and small surface decreased its areal capacitance value. However, with higher potential, the oxidation layer was too thick and caused an unexpected drop to the surface conductivity. The charge exchanging process at the surface became not so efficient, leading to an adverse impact to the capacitance. Thus, the 50 V applied potential could be considered as an optimal parameter for achieving suitable active material, surface area and conductivity.

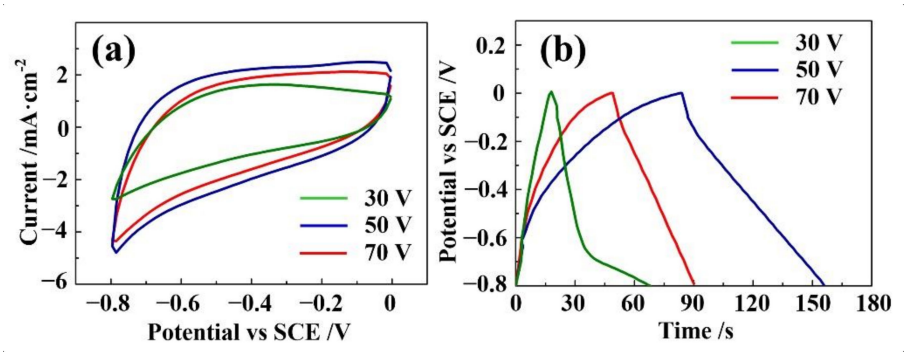

Figure 4. Capacitance performances of NASS samples with different anodic oxidation potential. (**a**) CV curves at scan rate of 100 mV·s^{-1}. (**b**) GCD curves at current density 1 mA·cm^{-2}.

The nitrogen doping processes were performed on the optimal 50 V anodic NASS samples reported above. Figure 5a depicts the CV curves of NASS-N sample at scan rates from 10 to 100 mV·s^{-1}. No obvious redox peak was found even at low scan rate, indicating its EDLC characteristic. Furthermore, the good symmetrical characteristic of CV curves proved reliable electrochemical reversibility of NASS-N samples. Figure 5b shows their GCD curves at current density of 0.5, 1.0, 2.0 and 5.0 mA·cm^{-2}. The nearly isosceles triangle shape and no obvious potential plateau further confirmed that the EDLC characteristic of NASS-N sample. The areal specific capacitance decreased with increasing current density due to the limited ion diffusion. At a commonly used current density (1.0 mA·cm^{-2}) [32,33], the NASS-N sample delivered an average areal capacitance of 321.3 mF·cm^{-2} (discharge time was 257 s). Figure 5c concludes the specific capacitances of NASS-N sample with different current densities. With increasing the current density, the calculated capacitance decreases. However, even the current density is changed from 0.5 mA·cm^{-2} to 8 mA·cm^{-2}, the capacitance is dropped from 330.7 mF·cm^{-2} to 250.3 mF·cm^{-2}, with 75.7% of the capacitance is retained. The result shows its good rate capability. A series of comparison of electrochemical measurements between NASS and NASS-N sample have been recorded and shown in Figure 5d–f. The CV curve of NASS-N shows much larger integral area than that of NASS sample (Figure 5d), indicating that much higher capacitance was achieved by nitrogen doping process. The detail value was calculated from GCD curves (Figure 5e): NASS-N samples had an average areal capacitance of 321.3 mF·cm^{-2}, while NASS-N samples had the value of 90 mF·cm^{-2}. The IR drop was also obtained from GCD curves [34]. For NASS samples, the value was relatively high at 0.10 V, resulting from the 11.9 µm-thick anodic oxidation layer. The value decreased to 0.04 V after nitrogen doping process. Figure 5f demonstrates the Nyquist plots of the two samples. Both of them exhibited a quasi-semicircle in the high-frequency region and an inclined line in the low-frequency region. In the low frequency part, the slopes of the straight lines were both larger than 45°, confirming an ideal capacitive behavior of the samples [35]. The NASS-N sample shows a steeper slope than that of NASS sample, indicating smaller Warburg impedance by nitrogen doping [36]. In the high frequency part, a significant decrease was observed in the radius of semicircle for the NASS-N sample, revealing much smaller charge transfer resistance (R_{ct} = 5.23 Ω), which can be contributed due to its improved conductivity by nitrogen doping process. As shown the intercept of the real axis in the high frequency range, both of the samples had relatively small equivalent series resistance of around 3.5 Ω), benefited from the good adhesion of SS substrate with active materials, and their nanopouors structure.

Figure 6 shows the cycling performance of the optimal NASS and NASS-N samples by repeating GCD cycles at a current density of 1 mA·cm^{-2}. A degradation in cyclic stability was observed by nitrogen doping process. After 500 cycles, 70% of the areal capacitance of NASS-N samples was preserved, while the residual capacitance of NASS samples was more than 84%. The inset in Figure 6b shows the first three and last three GCD cycles, indicating stable and smooth charge and discharge behavior. The coulombic efficiency

calculated from the consecutive charge and discharge process (Figure 6b) kept steady, with the value of 85.3% for NASS samples and 82.9% for NASS-N samples. These results agreed with Raut's [37] research on the similar SS-based supercapacitors.

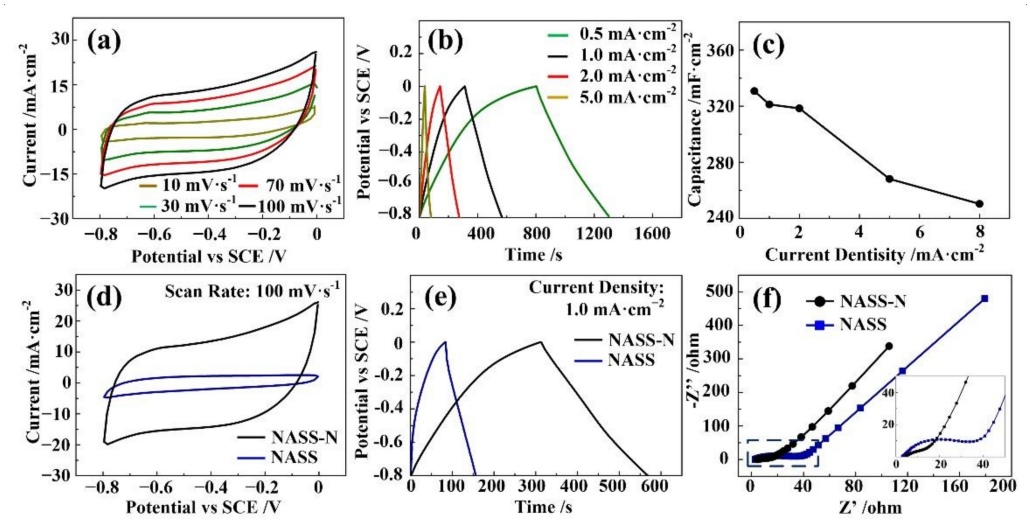

Figure 5. Capacitance performances of NASS-N sample. (**a**) CV curves at different scan rates. (**b**) GCD curves at different current densities. (**c**) Specific capacitances at different current densities. (**d**) CV curves at 100 mV·s^{-1} of NASS-N and NASS samples. (**e**) GCD curves at 1 mA·cm^{-2} of NASS-N and NASS samples. (**f**) Nyquist plots of NASS-N and NASS samples after cycling.

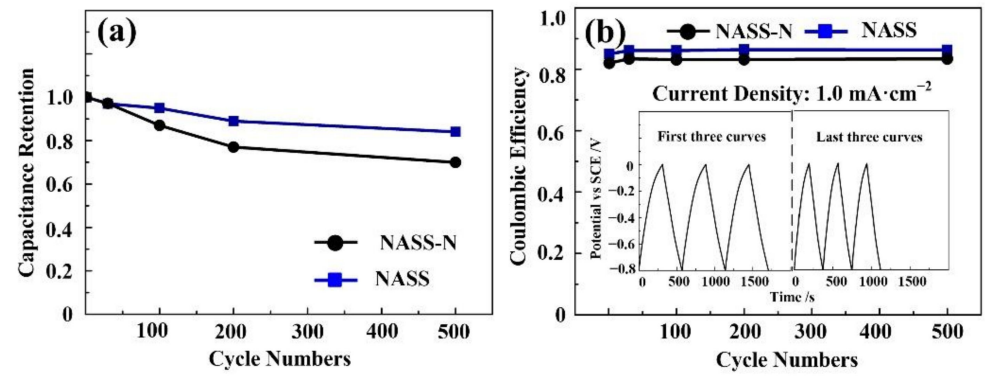

Figure 6. Cyclic performance of NASS-N and NASS samples at 1 mA·cm^{-2}. (**a**) Cyclic stability. (**b**) Coulombic efficiency, inset shows the first and last three GCD cycles of NASS-N samples.

The NASS sample shows a relatively high capacitance value compared with other report on Fe oxides [11–13,38], benefiting from its ultra-thick and unique nanoporous structure. The capacitance of NASS-N sample increases ~3.6 times after nitrogen-doping process through ammonia treatment. This improvement can be benefited from the mixed-anion compounds, especially the formation of Fe_3N nanosheets in NASS-N sample. In the ammonia atmosphere environment with high temperature, part of Fe_2O_3 in the nanoporous structure was reduced to Fe_3O_4, and was further transformed to Fe_3N. Compared with Fe_2O_3 or Fe_3O_4, Fe_3N had relatively low molecular weight and can transfer three electrons per formula unit as anode materials [39], and resulted in its high charge transfer efficiency. Moreover, Fe_3N also has high conductivity and good ionic diffusion due to the vacancies within their crystal structures [18]. Since Fe_3N nanosheets were planted in the nanoporous structure tightly, the charge carrier mobility of NASS sample can be improved accordingly, leading to smaller impedance in the Nyquist plots, smaller IR drops, as well as larger capacitance value. However, the excess oxygen vacancies caused by nitrogen doping process may lead to the poor cyclic stability [40,41]. The stability of NASS-N sample is still

needed for improvement in our future research by the possible methods like carbon shell deposition or glucose carbonization.

4. Conclusions

In summary, nanoporous oxide layers have been successfully fabricated on the surface of SS foil through anodization method for supercapacitor applications. The electrochemical anodization potential was optimized and 50 V oxidized sample showed the highest average areal capacitance. High temperature ammonia treatment was adopted for supercapacitive performance enhancement. The optimal thickness of nitrogen doped sample is ~11.9 μm. The morphological and structural characterization such as SEM, TEM, XRD and XPS concluded that Fe_3N nanosheets were existed in the oxide layer without any damage on its nanoporous structure. The nitrogen doped sample exhibited excellent supercapacitor performance with an areal capacitance as high as 321.3 $mF \cdot cm^{-2}$ at 1.0 $mA \cdot cm^{-2}$, which was 3.6 times than the figure of untreated sample, owing to improved charge transfer efficiency from Fe_3N nanosheets. The observations and discussions reported in this article may contribute to a better understanding of how to fabricate the high-performance, binder-free SS-based electrodes for supercapacitor usage in the view of constructing multiple anions compounds.

Supplementary Materials: The following supporting information can be downloaded at: https://www.mdpi.com/article/10.3390/ma15041615/s1, Figure S1: lower magnified SEM image of NASS sample.

Author Contributions: G.L. conceived and designed the experiments. W.Z. and J.X. performed the experiments and analyzed the data. W.Z. and K.W. wrote the paper. All authors have read and agreed to the published version of the manuscript.

Funding: This research was supported by the National Natural Science Foundation of China (51622507, 52005363 and 61471255), Natural Science Foundation of Shanxi Province, China (2016011040), and Scientific and Technological Innovation Programs of Higher Education Institutions in Shanxi Province, China (2016138).

Institutional Review Board Statement: Not applicable.

Informed Consent Statement: Not applicable.

Data Availability Statement: The data that support the findings of this study are available from the corresponding author upon reasonable request.

Conflicts of Interest: The authors declare no conflict of interest.

References

1. Lee, G.; Na, W.; Kim, J.; Lee, S.; Jang, J. Improved electrochemical performances of MOF-derived Ni–Co layered double hydroxide complexes using distinctive hollow-in-hollow structures. *J. Mater. Chem. A* **2019**, *7*, 17637–17647. [CrossRef]
2. Zheng, Y.; Zheng, S.; Xu, Y.; Xue, H.; Liu, C.; Pang, H. Ultrathin two-dimensional cobalt-organic frameworks nanosheets for electrochemical energy storage. *Chem. Eng. J.* **2019**, *373*, 1319–1328. [CrossRef]
3. Haider, W.A.; Tahir, M.; He, L.; Yang, W.; Minhas-Khan, A.; Owusu, K.A.; Chen, Y.; Hong, X.; Mai, L. Integration of VS2 nanosheets into carbon for high energy density micro-supercapacitor. *J. Alloys Compd.* **2020**, *823*, 151769. [CrossRef]
4. Huang, Y.; Buffa, A.; Deng, H.; Sarkar, S.; Ouyang, Y.; Jiao, X.; Hao, Q.; Mandler, D. Ultrafine $Ni(OH)_2$ nanoplatelets grown on 3D graphene hydrogel fabricated by electrochemical exfoliation for high-performance battery-type asymmetric supercapacitor applications. *J. Power Sources* **2019**, *439*, 227046. [CrossRef]
5. Maile, N.; Shinde, S.K.; Patil, S.S.; Kim, D.Y.; Fulari, A.V.; Lee, D.S.; Fulari, V.J. Capacitive property studies of electrochemically synthesized Co_3O_4 and Mn_3O_4 on inexpensive stainless steel current collector for supercapacitor application. *Ceram. Int.* **2020**, *46*, 14640–14649. [CrossRef]
6. Nuramdhani, I.; Gokceoren, A.T.; Odhiambo, S.A.; Mey, G.D.; Hertleer, C.; Langenhove, L.V. Electrochemical impedance analysis of a PEDOT:PSS-based textile energy storage device. *Materials* **2018**, *11*, 48. [CrossRef]
7. Amade, R.; Avetisyan, A.M.; Gonzalez, J.M.; Pino, A.P.; Gyorgy, E.; Pascual, E.; Andujar, J.L.; Serra, E.B. Super-capacitive performance of manganese dioxide/graphene nano-walls electrodes deposited on stainless steel current collectors. *Materials* **2019**, *12*, 483. [CrossRef]

8. Waghmode, R.; Jadhav, H.; Kanade, K.; Torane, A. Morphology-controlled synthesis of $NiCo_2O_4$ nanoflowers on stainless steel substrates as high-performance supercapacitors. *Mater. Sci. Energy Technol.* **2019**, *2*, 556–564. [CrossRef]
9. Mo, Y.; Meng, W.; Xia, Y.; Du, X.; Lin, Z.; Li, W. Facile flame deposit of CNFs/Fe_2O_3 coating on 304 stainless steel mesh and their high capacitive performance. *Electrochim. Acta* **2020**, *335*, 135527. [CrossRef]
10. Zhu, X.; Hou, D.; Tao, H.; Li, M. Simply synthesized N-doped carbon supporting Fe_3O_4 nanocomposite for high performance supercapacitor. *J. Alloys Compd.* **2020**, *821*, 153580. [CrossRef]
11. Sagu, J.S.; Wijayantha, K.G.U.; Bohm, M.; Bohm, S.; Rout, T.K. Anodized Steel Electrodes for Supercapacitors. *ACS Appl. Mater. Interfaces* **2016**, *8*, 6277–6285. [CrossRef] [PubMed]
12. Deshmukh, P.R.; Sohn, Y.; Shin, W.G. Flexible Solid-State Symmetric Supercapacitor Based on $(Fe,Cr)_2O_3$ Oxide Layer Developed on the Stainless Steel Mesh. *ACS Sustain. Chem. Eng.* **2018**, *6*, 300–310. [CrossRef]
13. Long, B.; Yang, H.; Wang, F.; Mao, Y.; Balogun, M.-S.; Song, S.; Tong, Y. Chemically-modified stainless steel mesh derived substrate-free iron-based composite as anode materials for affordable flexible energy storage devices. *Electrochim. Acta* **2018**, *284*, 271–278. [CrossRef]
14. Kageyama, H.; Hayashi, K.; Maeda, K.; Attfield, J.P.; Hiroi, Z.; Rondinelli, J.M.; Poeppelmeier, K.R. Expanding frontiers in materials chemistry and physics with multiple anions. *Nat. Commun.* **2018**, *9*, 772. [CrossRef] [PubMed]
15. Ansari, S.; Parveen, N.; Al-Othoum, M.; Ansari, M. Effect of Washing on the Electrochemical Performance of a Three-Dimensional Current Collector for Energy Storage Applications. *Nanomaterials* **2021**, *11*, 1596. [CrossRef] [PubMed]
16. Parveen, N.; Ansari, S.A.; Ansari, M.Z.; Ansari, M.O. Manganese oxide as an effective electrode material for energy storage: A review. *Environ. Chem. Lett.* **2021**, *20*, 283–309. [CrossRef]
17. Scaife, D. Oxide semiconductors in photoelectrochemical conversion of solar energy. *Sol. Energy* **1980**, *25*, 41–54. [CrossRef]
18. Balogun, M.-S.; Qiu, W.; Wang, W.; Fang, P.; Lu, X.; Tong, Y. Recent advances in metal nitrides as high-performance electrode materials for energy storage devices. *J. Mater. Chem. A* **2015**, *3*, 1364–1387. [CrossRef]
19. Wang, K.; Liu, G.; Hoivik, N.; Johannessen, E.; Jakobsen, H. Electrochemical engineering of hollow nanoarchitectures: Pulse/step anodization (Si, Al, Ti) and their applications. *Chem. Soc. Rev.* **2014**, *43*, 1476–1500. [CrossRef]
20. Wang, Y.; Li, G.; Wang, K.; Chen, X. Fabrication and formation mechanisms of ultra-thick porous anodic oxides film with controllable morphology on type-304 stainless steel. *Appl. Surf. Sci.* **2020**, *505*, 144497. [CrossRef]
21. Martin, F.; Del Frari, D.; Cousty, J.; Bataillon, C. Self-organisation of nanoscaled pores in anodic oxide overlayer on stainless steels. *Electrochim. Acta* **2009**, *54*, 3086–3091. [CrossRef]
22. Tsuchiya, H.; Suzumura, T.; Terada, Y.; Fujimoto, S. Formation of self-organized pores on type 316 stainless steel in organic solvents. *Electrochim. Acta* **2012**, *82*, 333–338. [CrossRef]
23. Albu, S.P.; Ghicov, A.; Schmuki, P. High aspect ratio, self-ordered iron oxide nanopores formed by anodization of Fe in ethylene glycol/NH4F electrolytes. *Phys. Status Solidi (RRL)—Rapid Res. Lett.* **2009**, *3*, 64–66. [CrossRef]
24. Farrag, H.H.; Sayed, S.Y.; Allam, N.K.; Mohammad, A.M. Emerging nanoporous anodized stainless steel for hydrogen production from solar water splitting. *J. Clean. Prod.* **2020**, *274*, 122826. [CrossRef]
25. Sarma, B.; Smith, Y.R.; Jurovitzki, A.L.; Ray, R.S.; Mohanty, S.K.; Misra, M. Supercapacitance behavior of porous oxide layer grown on 302 type stainless steel substrate. *J. Power Sources* **2013**, *236*, 103–111. [CrossRef]
26. Xia, S.; Du, W.; Zheng, L.; Chen, P.; Hou, Z. A thermally stable and easily recycled core–shell Fe_2O_3@CuMgAl catalyst for hydrogenolysis of glycerol. *Catal. Sci. Technol.* **2014**, *4*, 912–916. [CrossRef]
27. Takahashi, N.; Toda, Y.; Nakamura, T. Preparation of FeN thin films by chemical vapor deposition using a chloride source. *Mater. Lett.* **2000**, *42*, 380–382. [CrossRef]
28. Marco, J.F.; Herranz, T.; Gracia, M.; Gancedo, J.R.; Moutinho, F.; Prieto, P.; Sanz, J.M. Corrosion behavior under accelerated SO_2 corrosion tests of thin iron nitride films prepared by DIBS. *Surf. Interface Anal.* **2010**, *42*, 616–620. [CrossRef]
29. Yao, M.; Sun, B.; Wang, N.; Hu, W.; Komarneni, S. Self-generated N-doped anodized stainless steel mesh for an efficient and stable overall water splitting electrocatalyst. *Appl. Surf. Sci.* **2019**, *480*, 655–664. [CrossRef]
30. Zeng, Y.; Han, Y.; Zhao, Y.; Zeng, Y.; Yu, M.; Liu, Y.; Tang, H.; Tong, Y.; Lu, X. Advanced Ti-Doped Fe_2O_3@PEDOT Core/Shell Anode for High-Energy Asymmetric Supercapacitors. *Adv. Energy Mater.* **2015**, *5*, 1402176. [CrossRef]
31. Stoller, M.D.; Ruoff, R.S. Best practice methods for determining an electrode material's performance for ultraca-pacitors. *Energy Environ. Sci.* **2010**, *3*, 1294–1301. [CrossRef]
32. Zhan, Y.; Hu, Y.; Chen, Y.; Yang, Q.; Shi, Z.; Xiong, C. In-situ synthesis of flexible nanocellulose/carbon nano-tube/polypyrrole hydrogels for high-performance solid-state supercapacitors. *Cellulose* **2021**, *28*, 7097–7108. [CrossRef]
33. Yang, Y.; Zhang, D.; Liu, Y.; Shen, L.; Zhu, T.; Xu, X.; Zheng, J.; Gong, X. Solid-State Double-Network Hydrogel Redox Electrolytes for High-Performance Flexible Supercapacitors. *ACS Appl. Mater. Interfaces* **2021**, *13*, 34168–34177. [CrossRef] [PubMed]
34. Subramanian, V.; Zhu, H.; Wei, B. Synthesis and electrochemical characterizations of amorphous manganese oxide and single walled carbon nanotube composites as supercapacitor electrode materials. *Electrochem. Commun.* **2006**, *8*, 827–832. [CrossRef]
35. Hao, P.; Zhao, Z.; Tian, J.; Li, H.; Sang, Y.; Yu, G.; Cai, H.; Liu, H.; Wong, C.P.; Umar, A. Hierarchical porous carbon aerogel derived from bagasse for high performance supercapacitor electrode. *Nanoscale* **2014**, *6*, 12120–12129. [CrossRef]
36. Zhao, Y.; Chang, C.; Teng, F.; Zhao, Y.; Chen, G.; Shi, R.; Waterhouse, G.I.N.; Huang, W.; Zhang, T. Defect-engineered ultrathin δ-MnO_2 nanosheet arrays as bifunctional electrodes for efficient overall water splitting. *Adv. Energy Mater.* **2017**, *7*, 1700005. [CrossRef]

37. Raut, S.S.; Bommineedi, L.K.; Pande, S.; Sankapal, B.R. Prototype symmetric configured MWCNTs/Fe_2O_3 based solid-state supercapacitor. *Synth. Met.* **2021**, *271*, 116629. [CrossRef]
38. Nithya, V.; Arul, N.S. Review on α-Fe_2O_3 based negative electrode for high performance supercapacitors. *J. Power Sources* **2016**, *327*, 297–318. [CrossRef]
39. Li, Z.; Fang, Y.; Zhang, J.; Lou, X.W. (David) Necklace-Like Structures Composed of Fe3 N@C Yolk-Shell Particles as an Advanced Anode for Sodium-Ion Batteries. *Adv. Mater.* **2018**, *30*, e1800525. [CrossRef]
40. Tian, H.; Cheng, R.; Lin, M.; Li, P.; Lv, Y.; Ran, S. Oxygen-vacancy-rich ultrathin BiOBr nonosheets for high-performance supercapacitor electrodes. *Inorg. Chem. Commun.* **2020**, *118*, 108018. [CrossRef]
41. Liu, D.; Wang, C.; Yu, Y.; Zhao, B.-H.; Wang, W.; Du, Y.; Zhang, B. Understanding the Nature of Ammonia Treatment to Synthesize Oxygen Vacancy-Enriched Transition Metal Oxides. *Chem* **2019**, *5*, 376–389. [CrossRef]